Comparative Study on Microstructure and Aluminum Distribution Between Laser Beam Welding and Electron Beam Welding of Ti–6Al–4V Alloy Plates

Hengchang Bu[1] · Qiyu Gao[2] · Yun Li[1] · Feiyun Wang[1] · Xiaohong Zhan[1]

Abstract

Ti–6Al–4V alloy plates with a thickness of 4 mm were joined by electron beam welding (EBW) and laser beam welding (LBW). The comparison of LBW and EBW was performed according to grain morphology, microstructure, aluminum distribution, and microhardness of the joints. Results indicate that compared with LBW joint, more equiaxed grains are observed around the central zone of the EBW joint. The microstructure in fusion zone (FZ) of EBW joint presents more uneven with obviously coarser acicular martensite α′. Moreover, the aluminum element content of EBW joint is substantially lower, which demonstrates a more significant burning loss behavior in EBW process. The lower aluminum content in the upper center areas of the joints is attributed to the more significant element burning loss caused by higher temperature, whereas more uniform aluminum distribution in the upper part of the joints is ascribed to stronger convection form within the upper part of the joint. In addition, the characteristics of convection and thermal field within the molten pool are recognized as vital factors influencing the aluminum distribution. The lower microhardness profile in FZ of the EBW joint is principally attributed to coarser acicular martensite α′ and lower aluminum element in EBW joint.

Keywords Electron beam welding · Laser beam welding · Titanium alloy · Microstructure · Burning loss · Microhardness

1 Introduction

Titanium has attracted extensive attention in national defense, automobile manufacturing, and biomedical industries owing to the low density and great mechanical properties [1–3]. In the group of many titanium alloys, Ti–6Al–4V, a type of α + β titanium alloy, represents one of the most extensively employed titanium alloys [4].

Thus, great attention has been attracted to the manufacturing of titanium alloys. Nonetheless, the welding of titanium alloys is difficult since titanium alloys can react easily with active gases at high temperatures, which ultimately reduces the mechanical properties of joints [5]. Therefore,

numerous methods have been adopted: resistance welding [6], gas tungsten arc welding (TIG) [7], friction stir welding [8], laser beam welding (LBW) [9] and electron beam welding (EBW) [10].

Among these methods, LBW and EBW have been considered to possess considerable adaptability and excellent ability in creating deep and narrow joints with minimal deformation for the manufacture of components in various fields [11, 12], which can be ascribed to extremely high energy concentration in LBW and EBW. Accordingly, EBW and LBW of Titanium alloy have attracted many researchers to conduct in-depth studies.

As for LBW, Akman et al. [13] studied the effect of pulsed LBW parameters for joining 3 mm thick titanium alloy. Moreover, the weld geometry was regulated by accurately adjusting the process parameters. Wang et al. [14] performed LBW of titanium alloy plates. The welded joint showed excellent mechanical properties when the test temperature reaches 450 °C. Gao et al. [15] compared TIG and LBW for the joining of titanium alloy. The samples welded by LBW possess higher aspect ratio, narrower weld bead, and smaller residual distortions. Blackburn et al. [16] investigated the conventional

✉ Xiaohong Zhan
xiaohongzhan_nuaa@126.com

1 College of Material Science and Technology, Nanjing University of Aeronautics and Astronautics, Nanjing 211106, China

2 College of Science, Nanjing University of Aeronautics and Astronautics, Nanjing 211106, China

cyclical behaviors in the keyhole during the LBW of titanium alloy. Yang et al. [17] predicted heat-affected zone (HAZ) characteristics by a finite element method in the laser heating of the Ti–6Al–4V plate, and a narrower HAZ was found when the laser scan speed increased.

EBW is considered as an appropriate way to weld titanium alloys, due to the high energy density and the ultra-high vacuum conditions, which avoids the reaction between titanium alloys and active gases at high temperatures. 17.5 mm thick Ti–6Al–4V alloy plates were successfully joined with EBW, and the joint has passed all the experimental testing, as investigated by Saresh et al. [18]. The influence of beam oscillations on fatigue lifetime of titanium alloys joints by EBW has been analyzed, as mentioned by Babu et al. [19]. Wang et al. [20] studied the microstructure of titanium alloys joints by EBW under different beam moving modes. Their results indicated that the linear moving mode promotes the formation of fine grains through the segregation of metal elements in the molten pool. Damage-tolerant Ti–6Al–4V alloy plates were joined with EBW as reported by Lu et al. [21].

Some researchers conducted comparative studies on EBW and LBW. Qi et al. [22] compared EBW and LBW of 0.5 mm thick pure titanium. Their results show that higher quality pure titanium joints can be obtained by EBW. Moreover, LBW and EBW Ti–5Al–5V–5Mo–3Cr were conducted by Pasang et al. [23], the columnar grains were observed in both joints.

Additionally, in the high energy beam welding process, the low-melting-point alloy elements burning loss contributes to the degradation of joint performance. Zhan et al. [24] studied the distribution of Mg elements in EBW of aluminum alloy. Their results indicate that the uneven distribution of magnesium element in the joints was caused by the burning loss behavior of magnesium element. Zhang et al. [25] explored the aluminum distribution of titanium alloy joints by LBW. The experimental results show that the microhardness of the joints with higher aluminum content presents much harder, which indicates that the aluminum content offers a great influence on the joint performance. Therefore, the investigation of aluminum distribution is helpful to provide a better understanding of the degradation of mechanical properties and burning loss behavior in high energy beam welding of titanium alloy.

In this study, LBW and EBW were utilized to join Ti–6Al–4V alloy plates with a thickness of 4 mm, respectively. Besides, the comparison of the two welding methods was conducted according to weld geometry, grain morphology, microstructure, aluminum distribution, and microhardness. Furthermore, the distribution characteristics of the aluminum element in both joints are further interpreted in the light of the characteristic of convection and thermal field within the molten pool, whereas the microhardness characteristics are accounted for according to the microstructure and aluminum content of both joints.

2 Materials and Methods

2.1 Materials and Apparatus

The parent metal adopted in the experiment is the Ti–6Al–4V plates with a thickness of 4 mm. The plates are machined into 100 mm × 50 mm. The welding direction is perpendicular to the transverse cross-section of the plates. Table 1 displays the composition of the parent metal alloy.

The diagrammatic sketch of experimental apparatuses for the two welding methods is illustrated in Fig. 1a and b, LBW is performed using a PG YLS-6000 laser, while the laser optical set up is attached on a KUKA KR30HA commercial robot. The 99.99% pure argon at 11 L/min flow rate is employed for the purpose of shielding. In addition, the ZD150-30A EBW machine is adopted in the EBW experiment. The apparatuses present excellent performance under the selected process parameters. Diagrammatic sketch of high energy beam welding is illustrated in Fig. 2.

2.2 Experimental Procedure and Specimen Preparation

Table 2 shows the selected welding parameters applied to the LBW and EBW joints. Before the welding process, the weldments are cleaned by mechanical grinding in order to eliminate the inclusion of impurities. After the welding experiment, the samples (15 mm × 10 mm × 4 mm) are cut along the welding direction with a linear cutting machine. Then digital photographs were employed to obtain the macro morphology of the joint cross-section. The metallographic specimens were prepared by mounted, polished and etched employing Kroll's reagent. Micro-Vickers' hardness profiles of the joints were attained with a microhardness tester (HXS-1000A) under a test load of 500 N for 10 s.

Table 1 Composition of Ti–6Al–4V alloy (mass fraction, wt%)

Element	Al	O	Fe	V	C	N	H	Ti
Ti–6Al–4V	5.5–6.8	0.2	< 0.3	< 3.5–4.5	< 0.1	< 0.05	< 0.01	Bal.

Fig. 1 Diagrammatic sketch and experimental apparatus of LBW and EBW. **a** LBW, **b** EBW
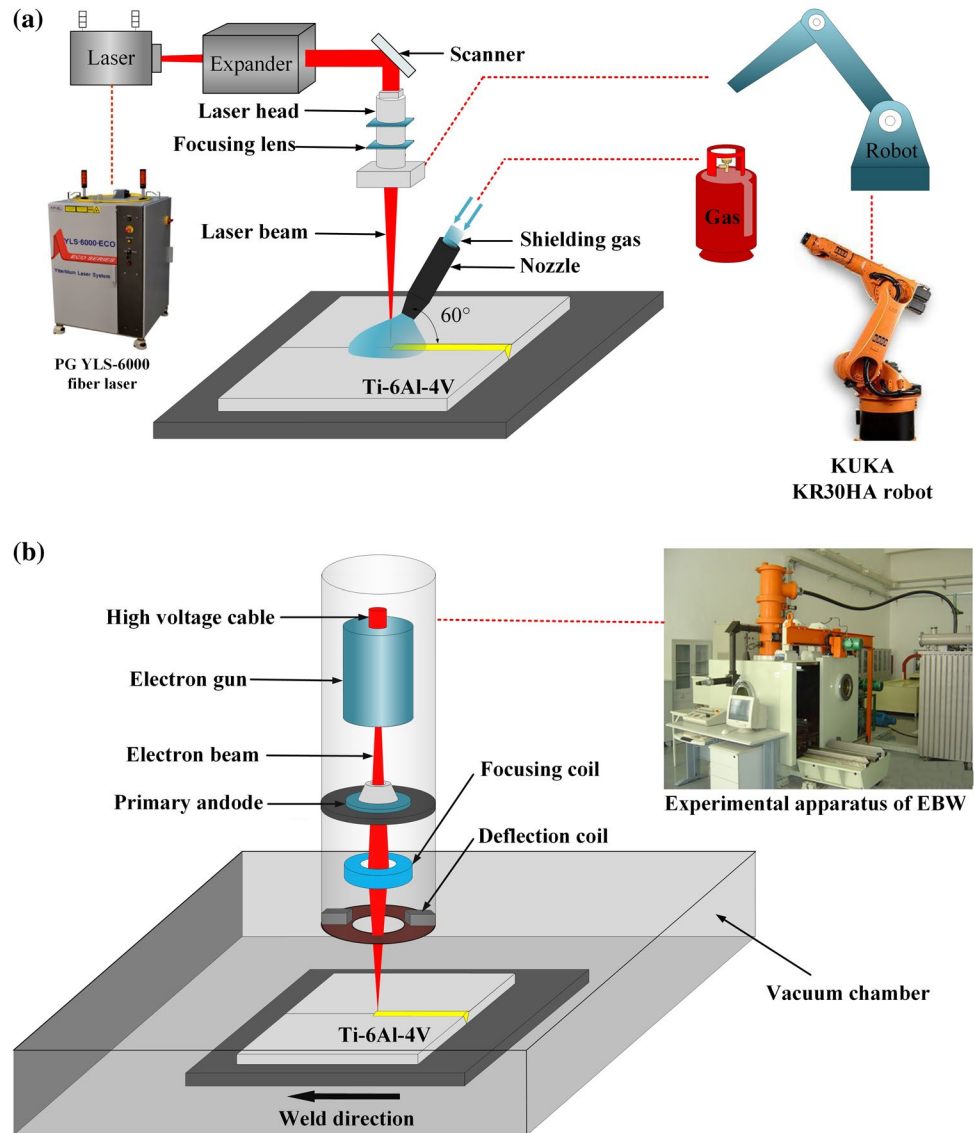
3 Results and Discussions

3.1 Morphology of the Joints

The macroscopic view of the joints by LBW and EBW is displayed in Fig. 3. It is clearly noticed that the full penetration joints were attained by LBW and EBW processes under the selected parameters. As displayed in Fig. 3, there are three different zones: consists of parent metal (PM), fusion zone (FZ) and HAZ. Both weld beads were fully penetrated. Furthermore, the upper surfaces of the two weld beads are recessed owing to the impact of the high energy beam and the recoil pressure induced by metal vaporization.

For the purpose of exploring the influence of two welding methods on the morphology of the joints, several variables were introduced to describe the geometric characteristics of welds: bottom bead width (BBW), top bead width (TBW) and concavity depth (CD). The results are exhibited in Fig. 4c. Meanwhile, it is clearly observed from Fig. 4a and b that the HAZ and FZ of the two joints are quantitatively measured at intervals of 0.5 mm along the vertical direction.

It is clearly found that the FZ width and HAZ width for EBW joint present obviously narrower compared to those in LBW joint, while the width range of HAZ and FZ in the EBW joint is also narrower. The analysis considers that the difference in energy density and heat transfer mechanism might be responsible for this. The higher energy density for EBW leads to a denser isotherm distribution in the EBW process, which ultimately contributes to a narrower HAZ and FZ. It is clearly found in Fig. 4a that the narrowest widths of weld bead are observed in the middle portion of the two joints. LBW and EBW joints share similar macro-morphology characteristics with the results in Refs. [21, 26].

Fig. 2 Schematic diagram of high energy beam welding: **a** 3D view; **b** side view; **c** top view
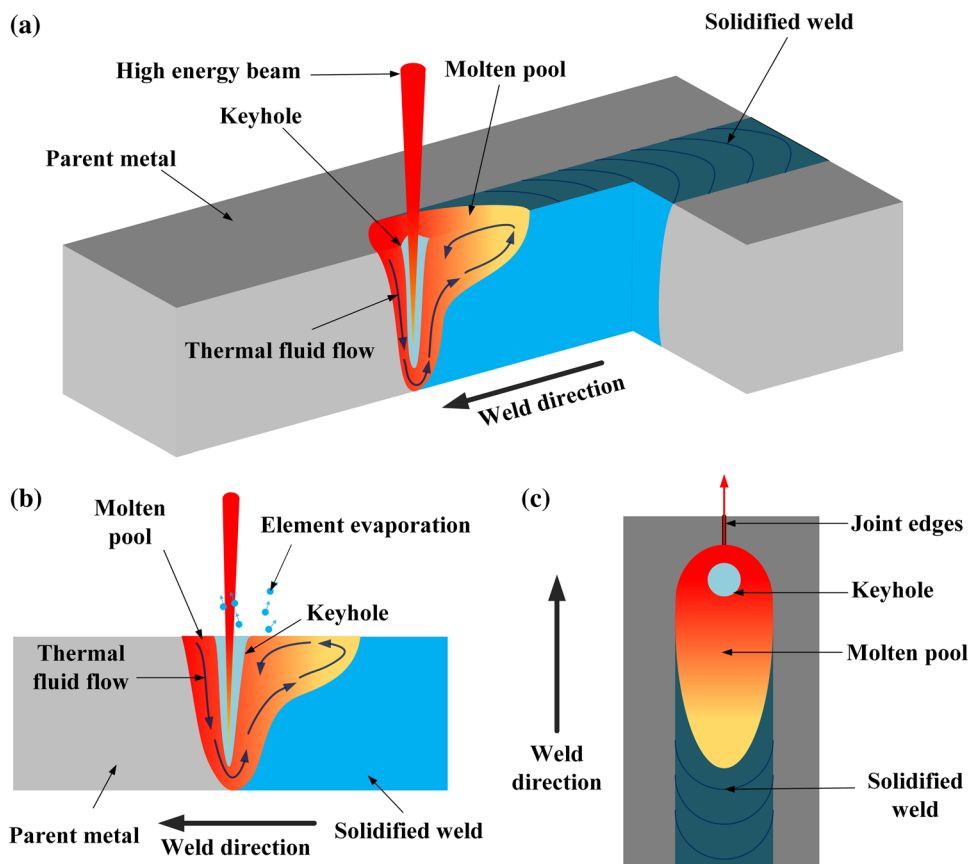

Table 2 Parameters of the welding experiment

Welding method	Parameters	Value
LBW	Laser power	4000 W
	Defocus	− 0.8 mm
	Welding speed	5.8 m/min
	Flow rate	13 L/min
EBW	Acceleration voltage	38 kV
	Electron beam current	18 mA
	Welding speed	1.6 m/min
	Vacuum degree	6.5×10^{-4} mbar

3.2 Microstructure of the Joints

Figure 5 delineates the grain morphology of LBW and EBW joints. As displayed in Fig. 5c, h, i, columnar grains epitaxially grow towards the central zone from the weld fusion line in both two joints. Moreover, in the center of the two joints, equiaxed grains are observed in Fig. 5c, f, h. These results are similar to the observation results in Refs. [21, 27].

In addition, it is easily noticed that the grain morphology at the center of LBW and EBW joints is highly different. As displayed in Fig. 5d and g, the columnar grains in the upper
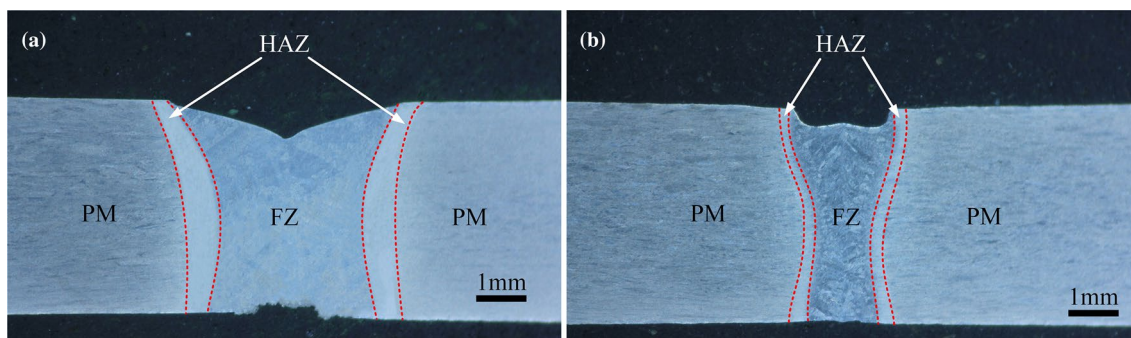

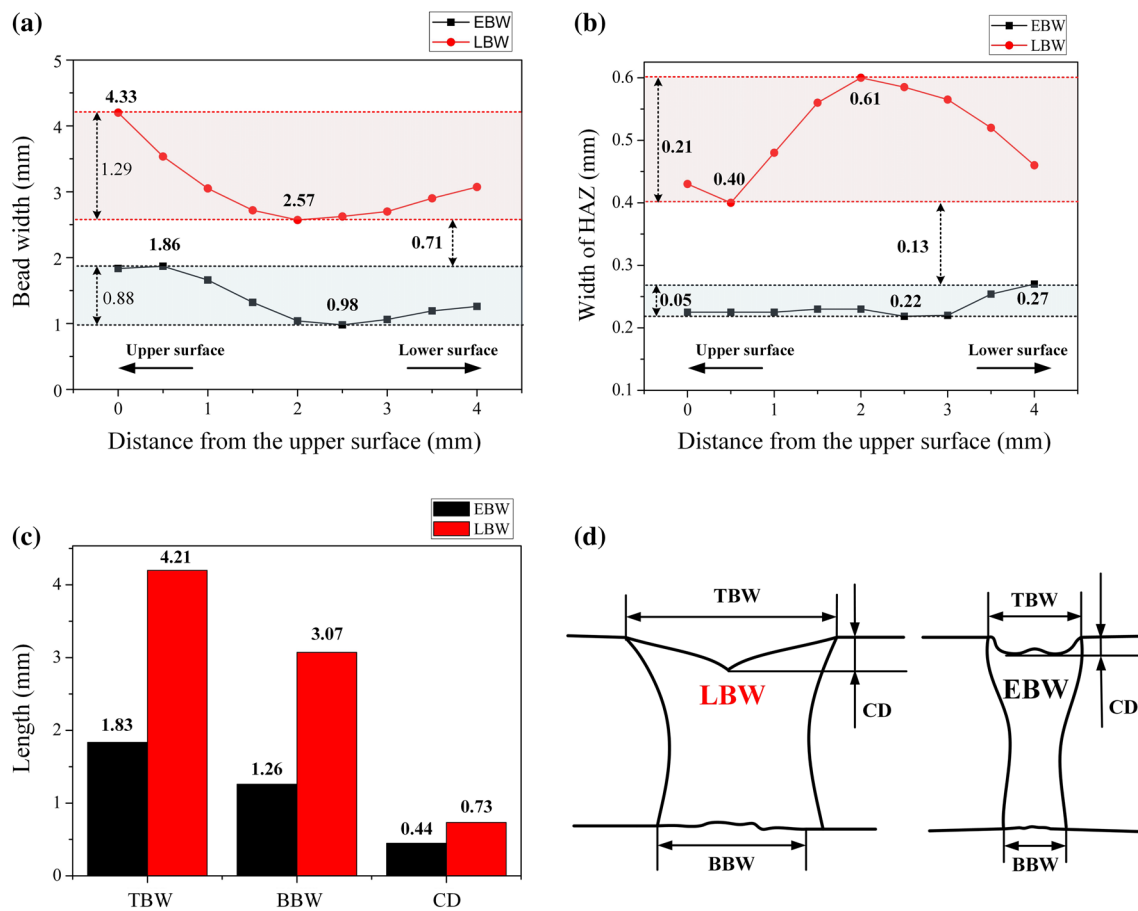**Fig. 3** Macro morphology of the joint cross-section. **a** LBW, **b** EBW

Fig. 4 Measured geometrical characteristics of the welds. **a** Width of the weld beads, **b** width of HAZ, **c** bottom bead width, top bead width and concavity depth; **d** measurement methods of the weld bead

part of the LBW joint present coarser compared to that of the EBW joint. Furthermore, it is observed in Fig. 5e and h that the main grain morphology in the lower central part of the LBW joint is equiaxed grain, whereas the principal grain morphology in the lower central part of the EBW join is columnar grain, as presented in Fig. 5f and i.

Hence, the epitaxial growth around the fusion line for columnar grain and the heterogeneous nucleation in the molten pool center for equiaxed grain are two major solidification ways. The grain morphological formation process is dominated by the competition between heterogeneous nucleation and epitaxial growth [28].

The grain morphology is substantially dominated by the constitutional supercooling within the molten pool. The boundary condition of constitutional supercooling is shown as follows [29].

$$\frac{G}{R} \le \frac{mC_0}{D}\left(\frac{1-k_0}{k_0}\right), \tag{1}$$

where G refers to the thermal gradient in the molten pool, R represents solidification velocity, C_0 is solute concentration, m means the liquid gradient of the equilibrium phase diagram, D refers to the coefficient of solute diffusion in the molten pool and k_0 represents solute distribution coefficient. Additionally, C_0, G, and R are supposed to be the critical factors dominating the growth of grain [30]. The grain growth of LBW and EBW is illustrated schematically in Fig. 6. Effects of C_0, R and G on grain growth in the welding process are displayed in Fig. 6e. At the fusion line of the joint, the degree of the supercooling within the liquid phase presents lower as a result of the lower R and higher G at the boundary of the molten pool. As such, it is found in Fig. 6e that the epitaxial growth is the principal grain growth mechanism and the formation of columnar grains occurred at the fusion line of the joint [28]. In the central zone of the joint, higher R and lower G lead to higher supercooling within the molten pool. Therefore, the principal grain formation mechanism within the central zone of the joint represents heterogeneous nucleation, eventually contributing to the growth of equiaxed grains.
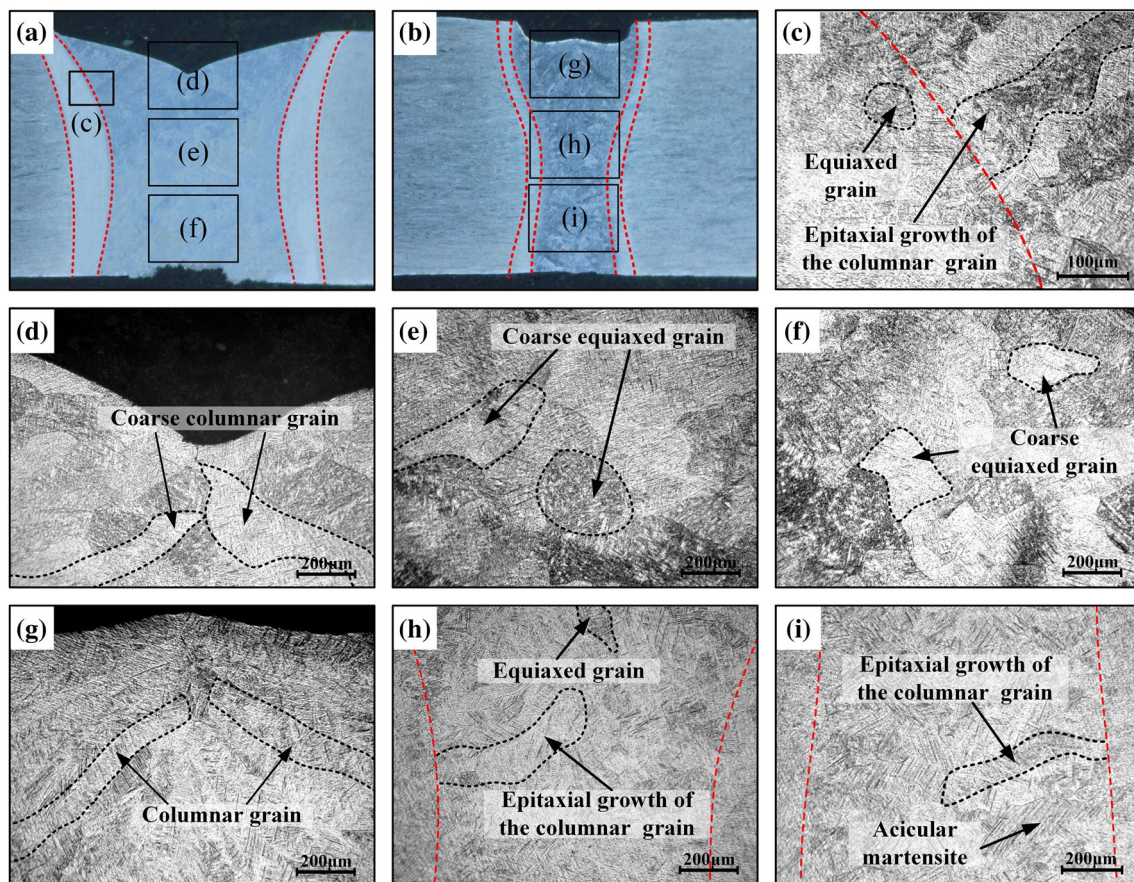
Fig. 5 Grain morphology of EBW and LBW joints: **a** macroscopic view of LBW joint, **b** macroscopic view of EBW joint, **c**–**f** metallography marked in **a**, **g**–**i** metallography marked in **b**

Nevertheless, compared with the LBW joint, there are much fewer equiaxed grains around the central area of EBW joint. It is clearly found in Fig. 6a, b that the solute concentration C_0 around the central area of EBW joint shows lower, owing to more significant evaporation of metal elements in EBW joint, which will be interpreted in the following section. Meanwhile, the energy density of the electron beam is generally considered to be higher than that of laser beam [31]. Consequently, it can be informed that the EBW isotherms present denser and the thermal gradient G shows higher. As such, lower C_0 and higher G in the molten pool results in lower supercooling, which inhibits the equiaxed grains from forming in the central zone of the EBW joint. Overall, the significant dissimilarity in grain morphology between EBW and LBW joints is ascribed to the different degrees of element burning loss and different thermal gradients within the molten pool.

The FZ and PM of the weld joint are observed with EDS and SEM. The microstructures of LBW and EBW joints are presented in Figs. 7 and 8 respectively. It is found in Fig. 7b that primary α + β phases are the main microstructure in PM of the joint. Figure 7d displays the composition of the

parent metal measured by EDS. Meanwhile, It can be also found from Figs. 7(c) and 8b–e that the microstructure in FZ for both LBW and EBW joints is substantially made up of acicular martensite α′ structure. The results are consistent with previous researches by Kashaev et al. [27] and Wang et al. [20].

Additionally, it is observed from Figs. 7c and 8e that compared with LBW joint, the microstructure of EBW joint shows more uneven, whereas the acicular martensite of EBW joint is comparatively coarser. Moreover, it is easily noticed from Figs. 7d and 8f that the aluminum content in FZ of EBW joints is moderately lower than that of PM, which implies that the burning loss of aluminum occurs in high energy beam welding process.

It is well known that the thermal cycle is highly vital in the microstructure formation of welded joints. As high power density beam welding methods, both EBW and LBW processes offer features of steep peak temperature, tremendously rapid heating and cooling velocity. In EBW and LBW processes of titanium alloy, the peak temperature is supposed to be greater than the melting point of the PM, while it is greater than β transus temperature as well.

Fig. 6 Diagrammatic sketch of grain growth: **a** heating process of LBW; **b** heating process of EBW; **c** grain morphology distribution in cooling process of LBW; **d** grain morphology distribution in cooling process of EBW; **e** influence of G, C_0 and R on the grain morphology [30]; **f** local enlargement of **b**
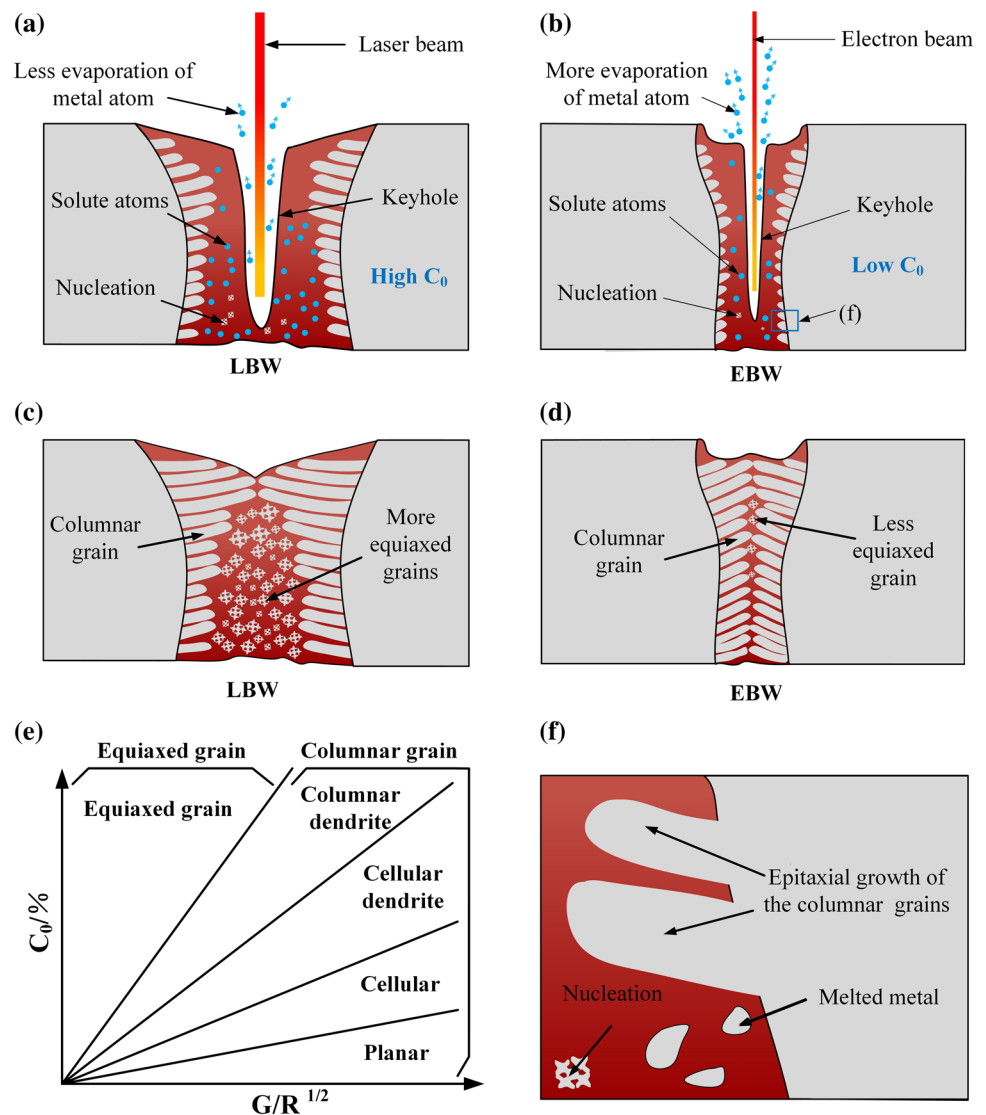
Thus, when parent metal is entirely melted, the primary α phase can be utterly transformed into β phase. However, as a result of the rapid cooling rates, the cooling time is too short to transform β phase into stable α phase since the transformation is primarily accomplished by atomic diffusion. Accordingly, the acicular martensite is ultimately produced within the molten pool when the shear transformation occurred on β phase [32]. The difference in microstructure between PM and FZ is mainly attributed to the different cooling rates [33]. More concentrated heat input in EBW process is recognized as a vital factor resulting in coarser acicular martensite of the EBW joint. In addition, the cooling rate of LBW process is generally considered to be higher than that of EBW process [34], which makes the martensite do not have enough time to coarsen in LBW process of Ti–6Al–4V alloy, thereby leading to finer acicular martensite in FZ of LBW joint.

3.3 Comparative Analysis of Aluminum Element Distribution

For the purpose of further exploring the influence of EBW and LBW on the element distribution of the welded joint, microzone composition detection is carried out along the vertical and horizontal directions of the weld beads. During EBW and LBW of Ti–6Al–4V, the operating temperatures can easily reach over 3000 °C [35, 36], which is well above the relatively low boiling point of aluminum (2467 °C [37]). Therefore, it can be speculated that there is a certain degree of aluminum burning loss in form of vapor during the high energy beam welding of Ti–6Al–4V alloy [25, 38]. In addition, little titanium and vanadium vapors could escape from the melted metal since the boiling points of titanium and vanadium are 3535 °C and 3380 °C respectively. The content of other elements in Ti–6Al–4V is much less than
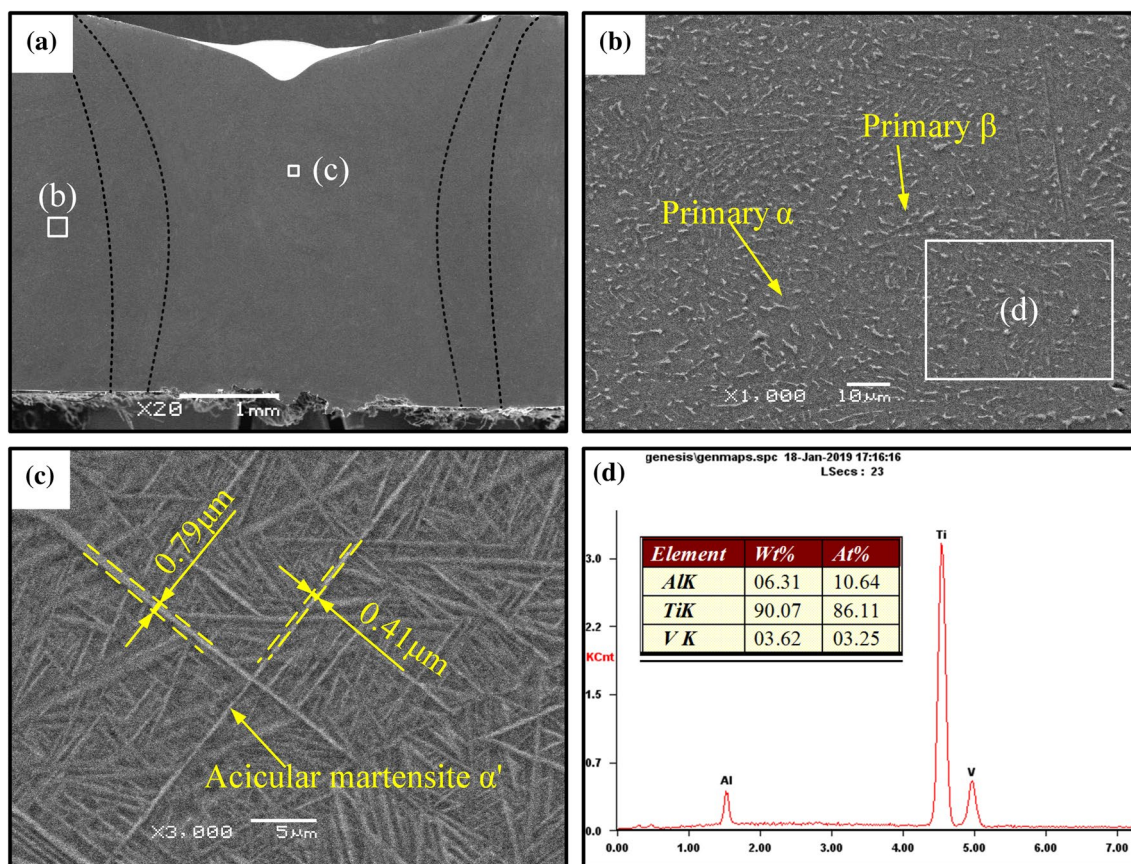
Fig. 7 Microstructure of LBW joint: **a** macroscopic view; **b** microstructure of PM in LBW joint; **c** microstructure of FZ in LBW joint; **d** element composition of PM marked in **b**

three principal elements (Ti, Al, and V). Hence, this paper mainly focuses on the difference in the aluminum burning loss behavior for LBW and EBW joints. Detection of microzone composition alone the vertical direction is implemented at intervals of 0.4 mm, while the distance between the highest detected microzone and the upper surface is 1 mm as depicted in Fig. 9.

Figure 9 displays the distribution of aluminum along the centerline of EBW and LBW joints. It is clearly noticed from Fig. 9 that the aluminum content in the FZ is substantially lower than that of the PM, which implies that burning loss of aluminum occurs in both EBW and LBW processes of Ti–6Al–4V alloy. For the EBW process, it is observed that the aluminum content increases as away from the upper surface of the joint. This implies that the burning loss of aluminum shows more significant around the upper portion of the joint, which is consistent with the burning loss behavior of magnesium of AA6061 EBW joint, as mentioned by Zhan et al. [24]. However, the content of aluminum in the LBW joint shows a significant fluctuation, where the content of aluminum in the middle part of the joint is lower than that of upper and lower ends. The fluctuation of aluminum content

along the weld centerline of the LBW joint is ascribed to the characteristic of thermal field and convection inside the molten pool.

Furthermore, it is informed from Fig. 9 that the aluminum content in the EBW joint represents basically lower than that in LBW joint except near the lower weld surface, which suggests that the degree of the aluminum burning loss in EBW joint shows far more remarkable than that in LBW joint. More conspicuous element burning loss behavior in EBW joints can be ascribed to higher peak temperature and denser isotherms caused by higher energy density electron beam. Moreover, the acicular martensite in the LBW joint with higher aluminum content present finer, which is in agreement with the results in Ref. [25].

Figure 10 represents the mass fraction of aluminum perpendicular to the centerline of EBW and LBW joints. Composition detection is carried out at distances of 1 mm as well as 1.8 mm from the upper surface of the joint, respectively. Overall, it is clearly observed that compared with LBW joint, the mass fraction of aluminum in EBW joint presents substantially lower, which verifies the previous conclusion that the burning loss of aluminum in the EBW joint is more
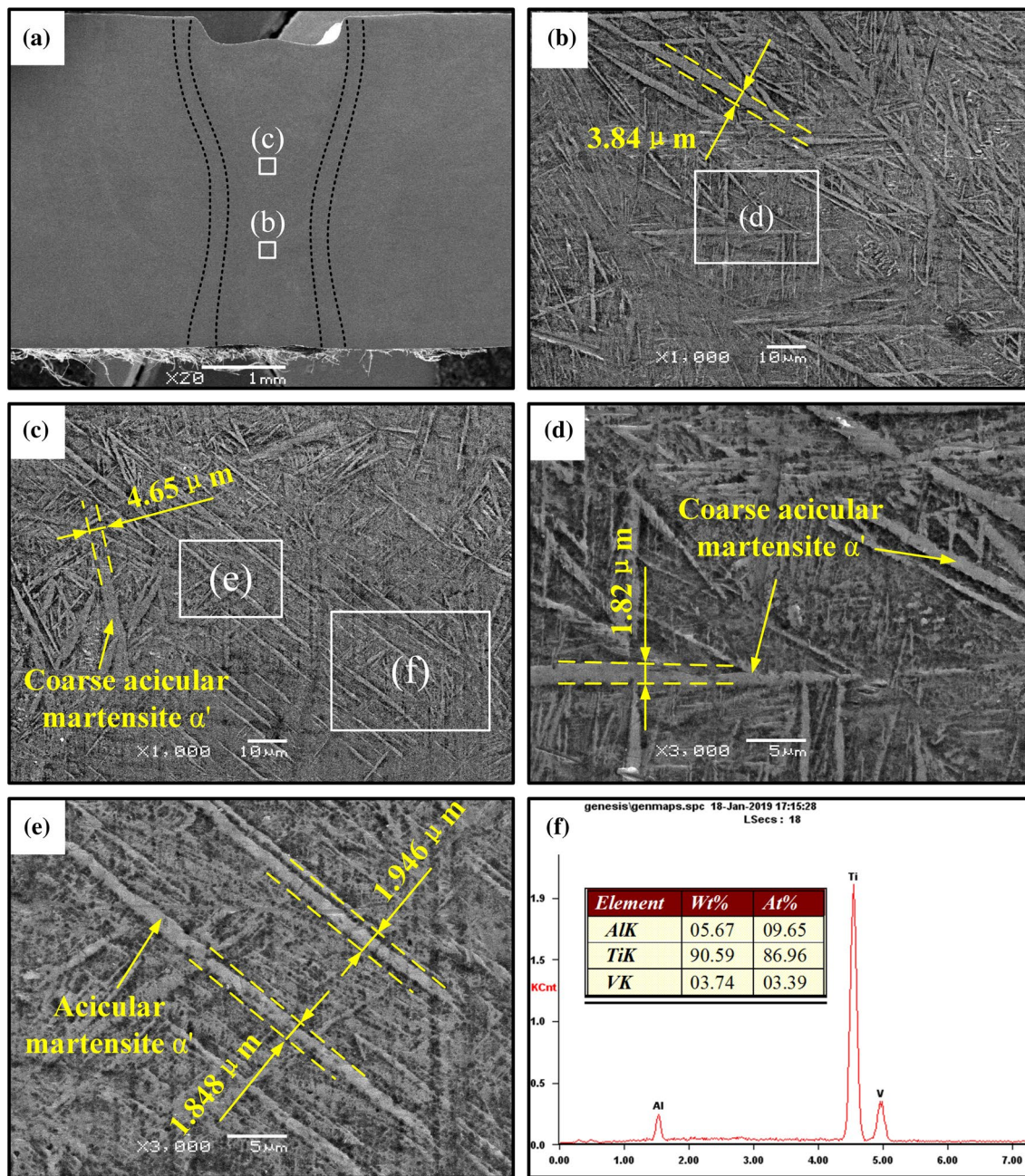
Fig. 8 Microstructure of FZ in EBW joint: **a** macroscopic view; **b**, **c** FZ marked in **a**; **d** FZ marked in **b**; **e** FZ marked in **c**; **f** composition of the FZ marked in **c**

conspicuous. Meanwhile, the aluminum content increases as away from the vertical weld centerline, which can be elucidated with the following statement: the low-melting-point alloy element evaporates from the keyhole during high energy beam welding process, thereby resulting in a lower content of this element along the weld centerline. As exhibited in Fig. 10, the aluminum content along the transverse direction of the upper weld is more uniformly distributed than that of the middle weld. Besides, the distribution of

aluminum in the upper part of the LBW joint is more uniform in comparison with that of EBW joint, which can be interrupted by the characteristic convection.

The aluminum distribution can be interpreted by the schematic representation in Fig. 11. The uneven spatial distribution of alloy elements in high energy beam welding is supposed to be associated with the thermal field and convection characteristic [39]. As illustrated in Fig. 11a and b, the formation of the dense isotherms in Gauss Distribution
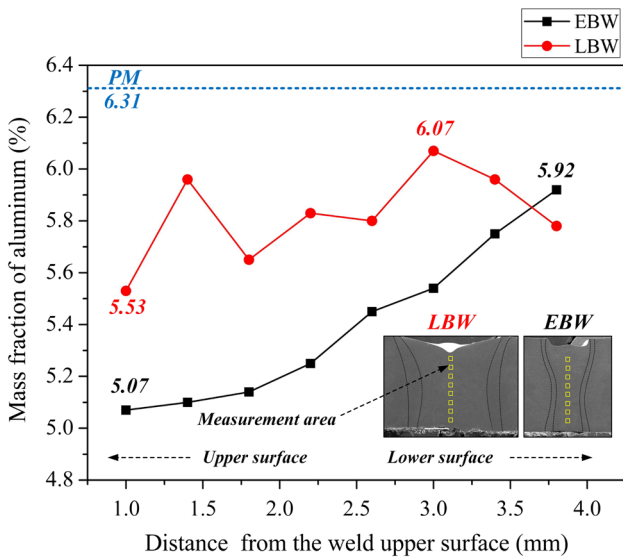
Fig. 9 Aluminum contents in the weld centerline

occurred inside the molten pool with the high energy beam. The temperature in the joint is defined as follows:

$$T_c = \frac{p_i}{\pi \lambda R_b},\qquad(2)$$

where P_i refers to the input power of the high energy beam, R_b is the radius of the heating area, and λ is related to the inherent properties of PM [24]. Thus, compared with the LBW process, the isotherm of EBW shows much denser with higher power density, resulting in a more conspicuous burning loss behavior.

During the LBW and EBW processes, intense convections, which contribute to the non-uniform spatial distribution of aluminum, are produced in the molten pool under the high energy beam impact forces and the thermal effect. Two principal convection behavior forms inside the molten pool present the Marangoni effect and the heat buoyance [40, 41]. The heat buoyance described below is formed by the density difference in various positions of the molten pool as a result of the thermal gradient.

$$f_b = -\rho g \beta (T - T_m),\qquad(3)$$

where T_m represents the melting point, β donates the thermal expansion coefficient, ρ represents the liquid density and g refers to the gravitational acceleration and [39, 42]. Besides, the relationship between β and temperature is given below:

$$\beta = -\frac{1}{\rho}\frac{\partial \rho}{\partial T},\qquad(4)$$

Under the action of the high energy beam, the molten metal around the keyhole has high temperature and low density. Besides, the melted metal around the fusion line possesses lower temperature and higher density owing to the decreased thermal effect. Therefore, as presented in Fig. 11c and d, the melted metal propelled by the heat buoyancy flows to the boundary and the upper surface from the keyhole of the molten pool.

Moreover, the Marangoni shear stress, which represents thermocapillary convection, is most pronounced around the joint surface. The Marangoni convection is represented below:
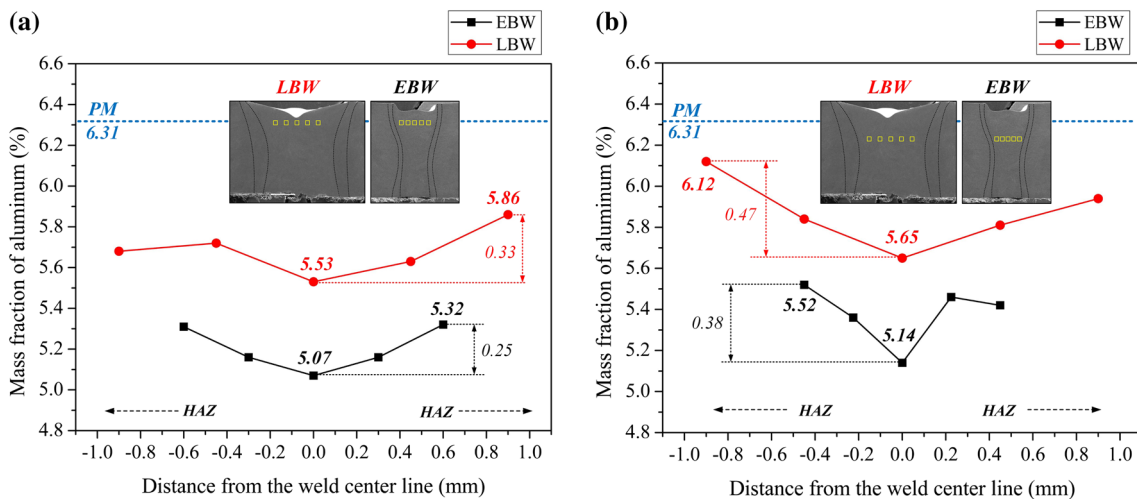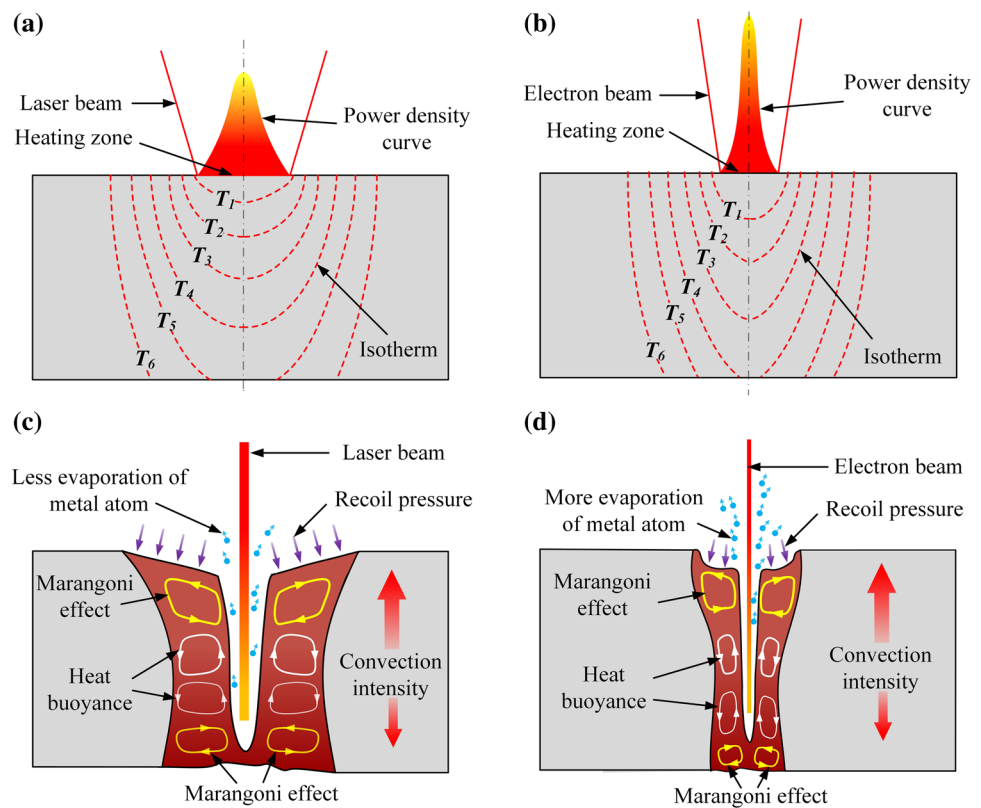

Fig. 10 Aluminum contents perpendicular to the centerline of the weld cross-section: **a** aluminum contents at distances of 1 mm from the upper surface of the joint; **b** aluminum contenst at distances of 1.8 mm from the upper surface of the joint

Fig. 11 Illustration of the isotherm and molten convection during EBW and LBW processes. **a** Isotherm in LBW joint; **b** isotherm in EBW joint; **c** diagram of the convection inside the LBW molten pool; **d** diagram of the convection inside the EBW molten pool

$$\eta \frac{\partial u}{\partial z} = \frac{\partial \gamma}{\partial T} \frac{\partial T}{\partial x} \tag{5}$$

$$\eta \frac{\partial v}{\partial z} = \frac{\partial \gamma}{\partial T} \frac{\partial T}{\partial y}, \tag{6}$$

where u and v represent the flow velocities in two vertical directions respectively, while γ refers to the surface tension [41, 43]. Compared with the central zone within the molten pool, the upper, lower and boundary in the molten pool have lower temperatures with higher surface tension. Thus, circulation is formed in the lower and upper portions of the joint with the action of surface tension and gravity. Marangoni convection near the upper surface presents much stronger compared to that near the lower surface owing to the higher-thermal gradient. Therefore, as illustrated in Fig. 11c and d, the convection characteristic within the molten pool embodies in two parts: Marangoni convection near the surface and the remainder convection driven by the heat buoyance [24]. Besides, the convection intensity presents stronger around the surface of the joint caused by the higher thermal gradient, thereby leading to a wider molten pool width.

Hence, the characteristics of isotherm and convection are recognized as principal factors that dominate the non-uniform aluminum distribution in LBW and EBW joints. The burning loss of aluminum element under high-temperature results in uneven aluminum element distribution within the

joint. The burning loss of elements in the higher temperature region shows more obvious, resulting in less aluminum content in this region. Therefore, the aluminum element content within the central and upper areas of the joint is lower as a result of higher temperature in these areas. Moreover, the more conspicuous aluminum burning loss behavior of EBW joint is ascribed to the higher temperature and denser isotherm in EBW process, as delineated in Fig. 11a and b. On the contrary, convection promotes the element distribution more uniform in the joint [44]. In comparison with the convection around the middle of the joint, Marangoni convection within the upper part of the joint presents stronger, contributing to a more uniform aluminum distribution in the upper part the joint.

3.4 Microhardness

Microhardness profiles in both joints are shown in Fig. 12. It indicates that the microhardness fluctuates appreciably as away from the weld centerline. Moreover, it is suggested that the microhardness in HAZ and FZ is harder than that in PM for both EBW and LBW joints, whereas the highest microhardness is in the HAZ. Deng et al. [32] and Kashaev et al. [27] both proposed that the microhardness values in HAZ and FZ in the high energy beam welded joints are higher than that in PM. As exhibited in Fig. 7, the microstructures in the FZ of the joints present martensite α′, while primary
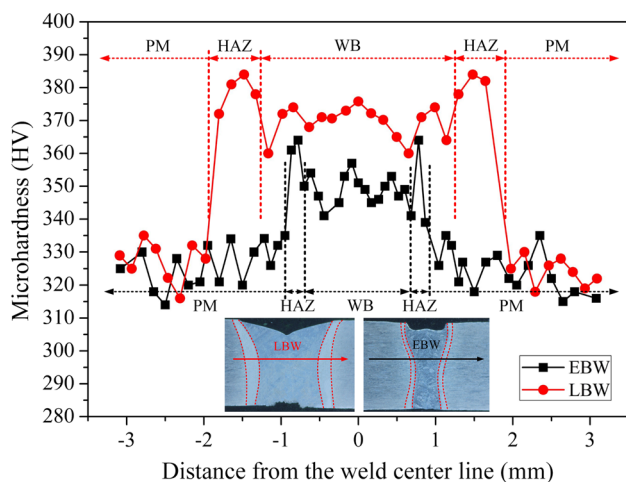
Fig. 12 Comparison of microhardness of LBW and EBW joints

α and primary β present the main microstructures of the parent metal. Furthermore, the transformed acicular martensite α + α′ phases are the principal microstructure in HAZ [32].

The microhardness of the existing phases in present titanium alloy is generally considered to be in this sequence: martensite α′ > α phase > β phase [45]. Therefore, it can be speculated that the microhardness in HAZ and FZ are harder than that in PM. The microhardness in HAZ presents marginally harder than that in FZ, mainly attributing to the dense martensite [18, 46]. It is evident that the microhardness values in HAZ and FZ of EBW joint present lower compared to that of LBW joint, which can be ascribed to coarser martensite α′ phase in the EBW joint. Lu et al. [21] reported that higher microhardness is attained by finer martensite in the EBW joint. Zhan et al. [24] investigated that the microhardness of EBW joint is also deeply influenced by the burning loss behavior. Consequently, the lower microhardness values in FZ and HAZ of EBW joint may also be ascribed to the lower mass fraction of aluminum in EBW joint. Overall, the microhardness profiles in FZ and HAZ of the EBW joint are supposed to be lower than that of LBW joint, mainly attributing to coarser acicular martensite α′ and lower mass fraction of aluminum in EBW joint.

4 Conclusion

(1) The β columnar grains epitaxially grow towards the weld centerline in both joints. The major grain morphology of LBW along the weld center line is equiaxed grain, while the principal grain morphology of EBW along the weld centerline present columnar grain.

(2) The microstructure in the EBW joint presents more uneven with the comparison of LBW joint. The acicular martensite in FZ of EBW joint presents obviously

coarser compared to that of the LBW joint, owing to the different thermal cycles of the LBW and EBW processes.

(3) The characteristics of isotherm and convection are recognized as principal factors that dominate the non-uniform aluminum distribution in LBW and EBW joints. The burning loss of aluminum in EBW joint is more conspicuous than that in LBW joint owing to higher temperature and denser isotherm in EBW process. Therefore, the aluminum element content within the upper and central areas of the joint is lower as a result of higher temperature in these areas.

(4) The aluminum of the upper weld is more uniformly distributed than that of the middle weld, which can be attributed to stronger Marangoni convection within the upper part of the joint in comparison with the convection within the middle part of the joint driven by the heat buoyancy.

(5) The microhardness of HAZ is marginally harder than those of FZ for two joints. The microhardness profile in FZ and HAZ of the EBW joint presents lower compared to that of LBW joint, mainly attributing to coarser acicular martensite α′ and lower aluminum content in EBW joint.

Compliance with Ethical Standards

Conflict of interest The authors declare no conflict of interest.

References

1. C. Leyens, M. Peters, *Titanium and Titanium Alloys* (Wiley, Weinheim, 2003)
2. H.J. Rack, J.I. Qazi, Titanium alloys for biomedical applications. Mater. Sci. Eng., C **26**, 1269–1277 (2006)
3. M.M. Dewidar, H.C. Yoon, J.K. Lim, Mechanical properties of metals for biomedical applications using powder metallurgy process: a review. Met. Mater. Int. **12**, 193–206 (2006)
4. Y. Zhang, J. Li, S. Che, Y. Tian, Electrochemical polishing of additively manufactured Ti–6Al–4V alloy. Met. Mater. Int. (2019). https://doi.org/10.1007/s12540-019-00556-0
5. K. Yonesawa, Welding of titanium and titanium alloys. Weld. Int. **1**, 1131–1142 (1987)
6. N. Kahraman, The influence of welding parameters on the joint strength of resistance spot-welded titanium sheets. Mater. Des. **28**, 420–427 (2007)
7. A.B. Short, Gas tungsten arc welding of α + β titanium alloys: a review. Mater. Sci. Technol. **25**, 309–324 (2009)
8. K. Gangwar, M. Ramulu, Friction stir welding of titanium alloys: a review. Mater. Des. **141**, 230–255 (2018)
9. D.H. Won, T.S. Bae, S. Ohkawa, F. Watari, The influence of output current on the tensile strength of laser-welded titanium joints. Met. Mater. Int. **9**, 493–496 (2003)

10. M.I. Utama, N. Park, E.R. Baek, Microstructure and mechanical features of electron beam welded dissimilar titanium alloys: Ti–10 V–2Fe–3Al and Ti–6Al–4V. Met. Mater. Int. **25**, 439–448 (2019)

11. A. Squillace, U. Prisco, S. Ciliberto, A. Astarita, Effect of welding parameters on morphology and mechanical properties of Ti–6Al–4V laser beam welded butt joints. J. Mater. Process. Technol. **212**, 427–436 (2012)

12. X. Yang, S. Li, H. Qi, Ti–6Al–4V welded joints via electron beam welding: microstructure, fatigue properties, and fracture behavior. Mater. Sci. Eng., A **597**, 225–231 (2014)

13. E. Akman, A. Demir, T. Canel, T. Sınmazçelik, Laser welding of Ti6Al4 V titanium alloys. J. Mater. Process. Technol. **209**, 3705–3713 (2009)

14. S. Wang, M. Wei, L. Tsay, Tensile properties of LBW welds in Ti–6Al–4V alloy at evaluated temperatures below 450°C. Mater. Lett. **57**, 1815–1823 (2003)

15. X.L. Gao, L.J. Zhang, J. Liu, J.X. Zhang, A comparative study of pulsed Nd: YAG laser welding and TIG welding of thin Ti6Al4 V titanium alloy plate. Mater. Sci. Eng., A **559**, 14–21 (2013)

16. J.E. Blackburn, C.M. Allen, P.A. Hilton, L. Li, M.I. Hoque, A.H. Khan, Modulated Nd: YAG laser welding of Ti–6Al–4V. Sci. Technol. Weld. Join. **15**, 433–439 (2010)

17. J. Yang, S. Sun, M. Brandt, W. Yan, Experimental investigation and 3D finite element prediction of the heat affected zone during laser assisted machining of Ti6Al4 V alloy. J. Mater. Process. Technol. **210**, 2215–2222 (2010)

18. N. Saresh, M.G. Pillai, J. Mathew, Investigations into the effects of electron beam welding on thick Ti–6Al–4V titanium alloy. J. Mater. Process. Technol. **192–193**, 83–88 (2007)

19. N.K. Babu, S.G.S. Raman, C.V.S. Murthy, G.M. Reddy, Effect of beam oscillation on fatigue life of Ti–6Al–4V electron beam weldments. Mater. Sci. Eng., A **471**, 113–119 (2007)

20. S. Wang, X. Wu, Investigation on the microstructure and mechanical properties of Ti–6Al–4V alloy joints with electron beam welding. Mater. Des. **36**, 663–670 (2012)

21. W. Lu, Y. Shi, Y. Lei, X. Li, Effect of electron beam welding on the microstructures and mechanical properties of thick TC4-DT alloy. Mater. Des. **34**, 509–515 (2012)

22. Y. Qi, J. Deng, Q. Hong, L. Zeng, Electron beam welding, laser beam welding and gas tungsten arc welding of titanium sheet. Mater. Sci. Eng., A **280**, 177–181 (2000)

23. T. Pasang, J.M.S. Amaya, Y. Tao, M.R. Amaya-Vazquez, F.J. Botana, J.C. Sabol, W.Z. Misiolek, O. Kamiya, Comparison of Ti–5Al–5 V–5Mo–3Cr welds performed by laser beam, electron beam and gas tungsten arc welding. Procedia Eng. **63**, 397–404 (2013)

24. X. Zhan, J. Chen, J. Liu, Y. Wei, J. Zhou, Y. Meng, Microstructure and magnesium burning loss behavior of AA6061 electron beam welding joints. Mater. Des. **99**, 449–458 (2016)

25. J. Zhang, R. Hu, S. Pang, A. Huang, Distribution of Al element of Ti–6Al–4V joints by fiber laser welding. Coatings **9**, 566 (2019)

26. C. Panwisawas, B. Perumal, R.M. Ward, N. Turner, R.P. Turner, J.W. Brooks, H.C. Basoalto, Keyhole formation and thermal fluid flow-induced porosity during laser fusion welding in titanium alloys: experimental and modeling. Acta Mater. **126**, 251–263 (2017)

27. N. Kashaev, V. Ventzke, V. Fomichev, F. Fomin, S. Riekehr, Effect of Nd: YAG laser beam welding on weld morphology and mechanical properties of Ti–6Al–4V butt joints and T-joints. Opt. Lasers Eng. **86**, 172–180 (2016)

28. T. Wang, Y.Y. Zhu, S.Q. Zhang, H.B. Tang, H.M. Wang, Grain morphology evolution behavior of titanium alloy components during laser melting deposition additive manufacturing. J. Alloys Compd. **632**, 505–513 (2015)

29. X. Zhan, H. Bu, Q. Gao, T. Yan, W. Ling, Temperature field simulation and grain morphology on laser welding-brazing between Ti–6Al–4V and 1050 aluminum alloy. Mater. Res. Express. **6**, 056551 (2019)

30. G. Li, M. Gao, C. Chen, C. Zhang, X.Y. Zeng, Characterisation comparison of laser and laser–arc hybrid welding of Invar 36 alloy. Sci. Technol. Weld. Join. **19**, 30–37 (2014)

31. X. Zhan, Y. Liu, J. Liu, Y. Meng, Y. Wei, J. Yang, X. Liu, Comparative study on experimental and numerical investigations of laser beam and electron beam welded joints for Ti6Al4 V alloy. J. Laser Appl. **29**, 012020 (2017)

32. Y. Deng, Q. Guan, B. Wu, J. Tao, A comparative study on electron beam welding and rigid restraint thermal self-compressing bonding for Ti6Al4 V alloy. Vacuum **117**, 17–22 (2015)

33. R.C. Picu, A. Majorell, Mechanical behavior of Ti–6Al–4V at high and moderate temperatures–Part II: constitutive modeling. Mater. Sci. Eng., A **326**, 306–316 (2002)

34. T.S. Balasubramanian, V. Balasubramanian, M.A. Muthumanikkam, Fatigue performance of gas tungsten arc, electron beam, and laser beam welded Ti–6Al–4V alloy joints. J. Mater. Eng. Perform. **20**, 1620–1630 (2011)

35. M. Akbari, S. Saedodin, D. Toghraie, R. Shoja-Razavi, F. Kowsari, Experimental and numerical investigation of temperature distribution and melt pool geometry during pulsed laser welding of Ti6Al4 V alloy. Opt. Laser Technol. **59**, 52–59 (2014)

36. M. Chiumenti, M. Cervera, N. Dialami, B. Wu, L. Jinwei, C. Agelet de Saracibar, Numerical modeling of the electron beam welding and its experimental validation. Finite Elem. Anal. Des. **121**, 118–133 (2016)

37. Y. Luo, H. Ye, C. Du, H. Xu, Influence of focusing thermal effect upon AZ91D magnesium alloy weld during vacuum electron beam welding. Vacuum **86**, 1262–1267 (2012)

38. S.V. Akhonin, N.P. Trigub, V.N. Zamkov, S.L. Semiatin, Mathematical modeling of aluminum evaporation during electron-beam cold-hearth melting of Ti–6Al–4V ingots. Metall. Mater. Trans. B **34**, 447–454 (2003)

39. M. Pastor, H. Zhao, R.P. Martukanitz, T. Debroy, Porosity, underfill and magnesium loss during continuous wave Nd: YAG laser welding of thin plates of aluminum alloys 5182 and 5754. Weld. J. (1999). http://img2.aws.org/wj/supplement/june99/PASTOR.pdf

40. K. Mundra, T. DebRoy, K.M. Kelkar, Numerical prediction of fluid flow and heat transfer in welding with a moving heat source. Numer. Heat Transf. Part A Appl. **29**, 115–129 (1996)

41. X. He, J.W. Elmer, T. DebRoy, Heat transfer and fluid flow in laser microwelding. J. Appl. Phys. **97**, 084909 (2005)

42. W. Zhang, C.H. Kim, T. DebRoy, Heat and fluid flow in complex joints during gas metal arc welding—Part I: numerical model of fillet welding. J. Appl. Phys. **95**, 5210–5219 (2004)

43. H. Zhao, T. Debroy, Weld metal composition change during conduction mode laser welding of aluminum alloy 5182. Metall. Mater. Trans. B **32**, 163–172 (2001)

44. S. Yan, S. Dong, B. Xu, Y. Wang, W. Ren, J. Fang, Effect of molten pool convection on pores and elements distribution in the process of laser cladding. Infrared Laser Eng. **43**, 2832–2839 (2014)

45. L. Zeng, T.R. Bieler, Effects of working, heat treatment, and aging on microstructural evolution and crystallographic texture of α, α′, α″ and β phases in Ti–6Al–4V wire. Mater. Sci. Eng., A **392**, 403–414 (2005)

46. B.D. Venkatesh, D.L. Chen, S.D. Bhole, Effect of heat treatment on mechanical properties of Ti–6Al–4V ELI alloy. Mater. Sci. Eng., A **506**, 117–124 (2009)